Despite the lack of eye-specific segregation of afferents after PND 9 to 25 activity blockade, the afferent projections were stereotyped in their patterning and did not represent a random diffuse projection to the entire LGN as when activity is blocked before development of segregation. Instead, the projections from both eyes were concentrated in a region similar to the normal location of lamina A (Fig. 4, C and D) and appeared to avoid lamina A1, indicating a substantial expansion and relocation of the afferent projection from the ipsilateral eye. This spatially restricted but unsegregated pattern suggests that there might be activity-independent cues in lamina A that are relatively attractive to axons from both eyes. In normal animals, activity-dependent competition occurs, and contralateral axons appear to have a competitive advantage, allowing them to take over the attractive real estate of lamina A and force the ipsilateral axons into lamina A1. Without competition, both eyes' axons would have equal ability to arborize in lamina A and select this region preferentially over lamina A1. The preferential arborization of axons in lamina A seen in this study was not observed in previous studies in which the development of segregation was prevented or retarded by activity blockade or enucleation before establishment of eye-specific layers (*3–5, 12, 13*). This difference could be explained if a preference for lamina A is established during the initial axonal segregation (PND 0–9) and requires a period of normal neuronal activity.

This study indicates that activity-dependent competition is vital not only for initial establishment of specific connections in the mammalian visual system but also for maintenance of these connections at least for some time during development. The possibility of attractive molecular cues or gradients in lamina A and the interactions between such cues and activity-dependent competition in normal development remain important open questions.

References and Notes

1. P. Rakic, *Nature* **261**, 467 (1976); C. J. Shatz, *J. Neurosci.* **3**, 482 (1983); D. W. Sretevan and C. J. Shatz, *J. Neurosci.* **6**, 234 (1986).
2. D. C. Linden, R. W. Guillery, J. Cucchiaro, *J. Comp. Neurol.* **203**, 189 (1981).
3. C. J. Shatz and M. P. Stryker, *Science* **242**, 87 (1988); D. W. Sretevan, C. J. Shatz, M. P. Stryker, *Nature* **336**, 468 (1988).
4. A. A. Penn, P. A. Riquelme, M. B. Feller, C. J. Shatz, *Science* **279**, 2108 (1998).
5. P. M. Cook, G. Prusky, A. S. Ramoa, *Vis. Neurosci.* **16**, 491 (1999).
6. Concerns about toxicity in the very young ferrets made the use of the sodium channel blocker tetrodotoxin impractical as a method for blocking retinal ganglion cell activity. All surgeries were performed according to protocols approved by the University of California at Davis Animal Care and Use Committee. Daily (24 ± 2 hours) eye injections of APB were done. Isofluorane anesthesia was used. Injections were made just posterior to the scleral margin with a 33-gauge needle on a Hamilton syringe. All subsequent injections were made into the same hole. APB dosages were calculated as described elsewhere (*9*). Injection volumes ranged from 1 to 2.8 μl. After the injections, animals received antibiotic ophthalmic ointment (Chloroptic) and prophylactic broad-spectrum antibiotics intramuscularly (Flocillin). The animals were returned to their mothers and littermates as soon as they awoke from the anesthesia (3 to 5 min).
7. In the adult retina, APB is a quite specific blocker of the ON-center pathway (*14*). However, in very young ferrets (PND 5 to 7) calcium imaging in vitro demonstrates that even very small concentrations of APB (1 μM) block all retinal ganglion cell spontaneous activity (Fig. 2). By PND 21, low concentrations of APB begin to have a more selective effect, but concentrations that fully block ON-center ganglion cells still decrease activity in OFF-center cells (*15*). The mechanisms by which APB blocks OFF-center activity in the young ferret retina are unknown.
8. APB-injected and normal age-matched control animals were euthnanized and perfused with 4% paraformaldehyde. Retinae were dissected out of the eyes, 1-mm "punches" were embedded in 5% agar, and 30-μm cross sections were cut on a vibratome. Sections were mounted on slides, stained for Nissl substance with thionin, cover-slipped, and photographed.
9. B. Chapman and I. Gödecke, *J. Neurosci.*, **20**, 1922 (2000).
10. Five microliters of 5% wheat germ agglutinin–horseradish peroxidase (WGA-HRP) (Sigma) was injected on PND 23 over a period of 5 min, following the same injection protocol used for the APB injections. Animals were euthanized 48 hours after the WGA-HRP injections and perfused with 4% paraformaldehyde. LGNs were embedded in gelatin/albumin and 50-μm vibratome sections were cut. Floating sections were reacted for HRP with a TMB protocol. Sections were mounted on slides, dried overnight, dehydrated, cover-slipped, and photographed. Ipsilateral and contralateral projections were measured with Scion Image software.
11. Animals were euthanized and perfused with 4% paraformaldehyde. LGNs were embedded in gelatin/albumin and 50-μm vibratome sections were cut. Sections were mounted on slides, dried overnight, dehydrated, Nissl-stained with cresyl violet, cover-slipped, and photographed.
12. R. W. Guillery, A. S. LaMantia, J. A. Robson, K. Huang, *J. Neurosci.* **5**, 1370 (1985).
13. D. W. Sretevan and C. J. Shatz, *J. Neurosci.* **6**, 990 (1986); J. B. Hutchins and V. A. Casagrande, *J. Comp. Neurol.* **298**, 113 (1990); J. Morgan and I. D. Thompson, *Vis. Neurosci.* **10**, 303 (1993).
14. M. M. Slaughter and R. F. Miller, *Science* **211**, 182 (1981); R. A. Shiells, G. Falk, S. Naghshineh, *Nature* **294**, 592 (1981).
15. W. T. Wong, K. L. Myhr, E. D. Miller, R. O. L. Wong, *J. Neurosci.* **20**, 351 (2000).
16. W. T. Wong and R. O. L. Wong, personal communication.

17. Supported by NIH grant EY-11369. E. Anderson, V. Chan, T. Hallam, and S. Shook collected pilot data. C. Wefers gave expert advice on retinal dissections and histology. A. Haines and S. Shah performed LGN measurements. L. Chalupa and L. Stone provided helpful comments on this manuscript.

1 June 1999; accepted 1 February 2000

Structure of the RNA Polymerase Domain of *E. coli* Primase

James L. Keck,[1] Daniel D. Roche,[2] A. Simon Lynch,[2]* James M. Berger[1]*

All cellular organisms use specialized RNA polymerases called "primases" to synthesize RNA primers for the initiation of DNA replication. The high-resolution crystal structure of a primase, comprising the catalytic core of the *Escherichia coli* DnaG protein, was determined. The core structure contains an active-site architecture that is unrelated to other DNA or RNA polymerase palm folds, but is instead related to the "toprim" fold. On the basis of the structure, it is likely that DnaG binds nucleic acid in a groove clustered with invariant residues and that DnaG is positioned within the replisome to accept single-stranded DNA directly from the replicative helicase.

All known polymerases synthesize nucleic acid in a 5′ to 3′ direction. This feature requires that the two antiparallel strands of DNA be replicated asymmetrically: The "leading" strand is made continuously at the replication fork, whereas the "lagging" strand is formed discontinuously. Because DNA polymerases are incapable of de novo initiation, cells use other mechanisms to prime DNA synthesis throughout replication. In 1971, Kornberg and co-workers proposed that DNA replication initiation required RNA transcription (*1*). Since then, replication-priming RNA polymerases (primases) have proven central to cellular and many viral replication mechanisms. Primases initiate leading-strand synthesis once and lagging-strand synthesis multiple times during the course of replication. Depending on the organism, primases exist either as individual proteins or as primase-helicase polyproteins; in almost all cases their activities are coupled to the replisome by protein-protein interactions with other replication factors (*2*).

Escherichia coli primase (DnaG) interacts with the replicative DnaB helicase, single-

[1]Department of Molecular and Cell Biology, University of California, Berkeley, 229 Stanley Hall, no. 3206, Berkeley, CA 94720, USA. [2]Tularik, 2 Corporate Drive, South San Francisco, CA 94080, USA.

*To whom correspondence should be addressed.

stranded DNA binding protein (SSB), and DNA polymerase III holoenzyme (*3–6*). Although DnaG is capable of synthesizing 60-nucleotide-long primers in vitro (*3*), this primer length is restrained to 11 (±1) nucleotides in the context of the replisome (*7*). During lagging-strand synthesis of the *E. coli* genome, DnaG proteins must transcribe ~2000 to 3000 RNA primers at a rate of about one primer per second (*8*). Homologs of DnaG have been identified in all prokaryotes, as well as in several bacteriophage. On the basis of sequence analysis, these proteins appear structurally distinct from primases known to act in archaeal and eukaryotic replication.

DnaG has been shown by proteolysis to comprise three structural domains: a 12-kD NH_2-terminal Zn^{2+}-binding domain (ZBD), a 36-kD core domain containing the polymerase region, and a 15-kD COOH-terminal DnaB-interaction domain (DnaB-ID) (*9*, *10*) (Fig. 1A). A recombinantly expressed DnaG core fragment including residues 111 to 433 (DnaG-RNAP) retains the ability to transcribe RNA in vitro, although with a reduced RNA polymerase activity (*11*). This domain is not expected to be functional during replication in vivo, as it lacks both the DnaB-ID and the ZBD (*9*).

Purified DnaG-RNAP was crystallized in two distinct forms, depending on whether YCl_2 or $SrCl_2$ was included in the crystallization conditions (*12*). The structure of DnaG-RNAP in the $SrCl_2$ cell was determined by multiwavelength anomalous dispersion (MAD) phasing (Fig. 1B) and was subsequently refined to 1.6 Å resolution (*13*). The YCl_2 form was solved by molecular replacement and refined to 1.7 Å resolution (*14*) (Table 1). Although a third crystal form grown in the presence of $DyCl_3$ was also obtained, these crystals diffracted to 2.5 Å and were used only for difference-Fourier analysis.

DnaG-RNAP is a modular, cashew-shaped molecule of dimensions 30 Å by 35 Å by 75 Å that is composed of three subdomains (Figs. 1C and 2A). The NH_2-terminal

Table 1. Data collection and refinement statistics.

Data collection

	Se-Met-λ1	Se-Met-λ2	Native	YCl_2	$DyCl_3$
Wavelength (Å)	0.9791	0.9537	1.050	1.000	0.9792
Resolution (Å)	20–2.5	20–2.5	20–1.6	20–1.7	20–2.5
(Last shell Å)	(2.59–2.50)	(2.59–2.50)	(1.66–1.60)	(1.76–1.70)	(2.59–2.50)
Reflections	76,292/	79,996/	182,728/	236,503/	68,334/
(measured/unique)	11,894	11,984	43,387	39,886	11,894
R_{sym}* % (last shell)	5.0 (14.5)	5.1 (13.8)	3.6 (17.7)	5.4 (28.7)	8.8 (26.3)
I/σ (last shell)	22.3 (14.1)	23.1 (15.7)	27.2 (4.0)	23.2 (3.7)	13.9 (5.1)
Completeness %	99.5 (96.7)	99.9 (99.7)	97.2 (94.9)	99.2 (94.6)	99.6 (99.6)
(last shell)					

Phasing statistics

	Se-Met-λ1	Se-Met-λ2	Refinement	Native	YCl_2
			Resolution Å	20–1.6	20–1.7
Phasing power†/R_{cullis}‡			R_{factor}/R_{free}§	23.1/27.6	20.9/26.3
(acentric)	1.12/0.79	0.00/1.23	rmsd bonds (Å)	0.006	0.008
(centric)	1.07/0.69	0.00/1.00	rmsd angles (°)	1.4	1.6
(anom)	0.71/0.77	0.99/0.68	#waters/#metals	234/1	290/4
Figure of merit	0.487				
(20–2.5 Å)					

*$R_{sym} = \Sigma\Sigma_j|I_j - \langle I\rangle|/\Sigma I_j$, where I_j is the intensity measurement for reflection j and $\langle I\rangle$ is the mean intensity for multiply recorded reflections. †Phasing power = $\langle F_h\rangle/E$, where $\langle F_h\rangle$ is the rms heavy-atom structure factor and E is the residual lack of closure error. ‡$R_{cullis} = \Sigma||F_{ph} \pm F_p| - |F_{h,c}||/\Sigma|F_{ph} \pm F_p|$, where $F_{h,c}$ is the calculated heavy-atom structure factor. §$R_{work,\ free} = \Sigma||F_{obs} - |F_{calc}||/|F_{obs}|$, where the working and free R factors are calculated using the working and free reflection sets, respectively. The free reflections (10% of the total) were held aside throughout refinement.

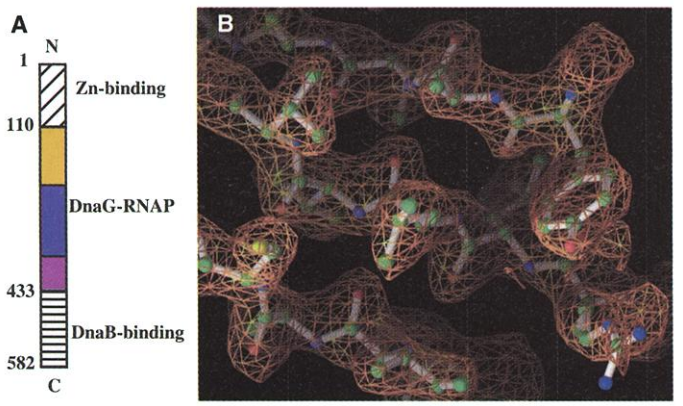

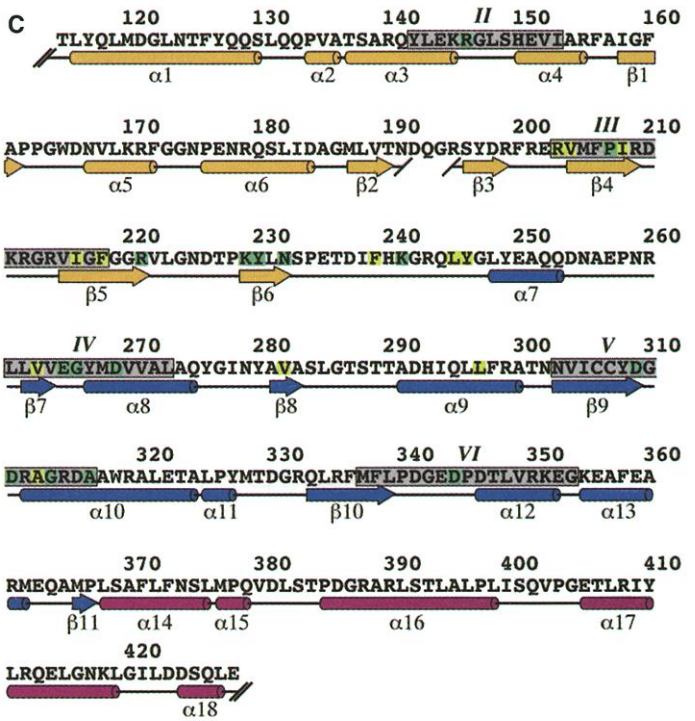

Fig. 1. Structural composition and experimental electron density of *E. coli* DnaG-RNAP. (**A**) Schematic diagram illustrating the domain boundaries of full-length *E. coli* DnaG (*9*, *10*). Gold, blue, and purple color coding on the DnaG-RNAP domain correspond to NH_2-terminal (residues 115 to 240), central (residues 241 to 367), and COOH-terminal (residues 368 to 428) subdomains in the structure, respectively. (**B**) Representative, solvent-flattened experimental electron density of three β strands within the toprim region of DnaG-RNAP. Contouring is at 1.4σ above the mean. The refined model is shown as a ball-and-stick representation. The figure was generated by Ribbons (*27*). (**C**) Secondary structure and conservation in DnaG-RNAP. The DnaG-RNAP sequence is highlighted to illustrate the positions of invariant (green boxes) and highly conserved (yellow boxes) residues as well as the locations of sequence motifs II to VI (*19*) (gray boxes). Sequence conservation was determined by comparing 28 bacterial primase proteins with ClustalX (*28*); "invariant" and "highly conserved" residues are defined by the Gonnet 250 weighting scheme (*29*). Secondary structure content of each subdomain is indicated below the sequence as cylinders (α helices), arrows (β strands), or lines (coil) and is color-coded as in (A). Abbreviations for the amino acid residues are as follows: A, Ala; C, Cys; D, Asp; E, Glu; F, Phe; G, Gly; H, His; I, Ile; K, Lys; L, Leu; M, Met; N, Asn; P, Pro; Q, Gln; R, Arg; S, Ser; T, Thr; V, Val; W, Trp; and Y, Tyr.

subdomain has a mixed α/β fold that is unique when compared to other proteins in the structural database [DALI (*15*)]. The central subdomain forms a five-stranded β sheet sandwiched by six α helices. Part of this region belongs to the toprim fold family, as had been predicted by Koonin and co-workers (*16*). The toprim fold has been observed in a variety of metal-binding phosphotransfer proteins, including nucleases, topoisomerases, and response regulators (*16*, *17*). The COOH-terminal subdomain comprises an antiparallel, three-helix bundle that is structurally similar to regions in a variety of unrelated proteins. The NH_2- and COOH-termini of DnaG-RNAP protrude from the same side of the protein and lie ~55 Å apart.

The toprim and NH_2-terminal subdomains abut each other to form a shallow, wedge-shaped cleft on the concave side of the protein (Fig. 2, B and inset). All 14 invariant, surface-exposed residues shared among bacterial primase RNAP domains cluster at this cleft surface (Fig. 3A). These residues belong to a series of conserved, primase-specific sequence motifs (*18*, *19*). Mutagenesis experiments have demonstrated that a number of these conserved groups are important for primase activity (*20*, *21*), implying that this region is critical for DnaG function.

In the YCl_2-containing crystals, three peaks of positive difference density (>3.5σ) were observed in the DnaG-RNAP cleft (Fig. 3B). These peaks lie only 2.4 to 2.5 Å from the carboxylates of two invariant acidic amino acids (Glu-265 and Asp-309) and are not observed in $SrCl_2$ crystals, implying that they represent Y^{2+} ions. The same binding surface of DnaG-RNAP also shows 7.5σ difference density in $DyCl_3$ cocrystals, further confirming that this region can bind metal ions. The acidic metal-liganding residues are part of the toprim region of DnaG-RNAP. Superposition of the toprim regions from Mg^{2+}-bound *Methanococcus jannaschii* topoisomerase VI (*22*) and Y^{2+}-bound DnaG-RNAP [root mean square deviation (rmsd) = 2.0 Å for 57 C_α atoms] shows that two of the Y^{2+} ions seen in our DnaG-RNAP structure bind near the Mg^{2+} position observed in topoisomerase VI (Fig. 3B). Primase activity is known to be metal-dependent, and mutation of the Glu-265 equivalent in the homologous P4 phage primase results in loss of activity (*20*), suggesting that this region of the cleft serves as the active site for RNA chain elongation in DnaG.

The use of metals by DnaG is consistent with cofactor requirements in other polymerases, but metal coordination in DnaG-RNAP does not use the "palm" metal-binding fold that is conserved among many other nucleic acid polymerases (Fig. 3C) (*23*). Instead, DnaG appears to use a simple phosphotransfer domain for metal coordination and thus represents a distinct structural class of polymerases. The structural differences between DnaG and "classic" polymerases may help explain the functional distinctions of primases, which include reduced processivity and lower fidelity (*2*).

If the cleft represents the catalytic center of DnaG-RNAP, how might this region bind DNA? In the DnaG-RNAP structure, the cleft diameter measures ~9 Å at one end and 20 Å at the other (Fig. 2, B and inset). The narrow mouth of the cleft contains several invariant basic residues (Arg-146, Arg-221, and Lys-229). The mouth opens up to a region that is lined by the metal-binding center from the toprim motif on one side and the highly conserved primase II and III motifs from the NH_2-terminal subdomain on the other. Beyond the catalytic region, the cleft broadens to a shallow depression that has both basic and hydrophobic character. We propose that single-stranded DNA (ssDNA) can be threaded through the narrow mouth and that the electrostatically positive ridge of the NH_2-terminal subdomain acts as an interaction surface for the template phosphodiester backbone. Synthesis would occur at the metal-binding site on the toprim side of the cleft, with the resulting RNA:DNA duplex extruded into the wide, shallow depression. Mutagenesis experiments in phage P4 (*20*), coupled with the observation that mutation of the invariant Lys-241 of *E. coli* DnaG permits transcription initiation but inhibits primer elongation (*21*), are together consistent with this scheme. This model for nucleic acid binding and synthesis would place the RNA:DNA hybrid proximal to the NH_2-terminus of DnaG-RNAP, near the predicted position of the ZBD of the intact DnaG protein.

Primer synthesis in bacteria is coupled to DNA replication by interactions between primase, the replicative helicase, and other replication factors. The precise mechanism by which these processes are coordinated at the molecular level has remained largely obscure. In *E. coli*, a noncovalent protein:protein interaction links the COOH-terminal domain of DnaG with the DnaB helicase (*9*) in a 6:1 helicase:primase complex. In T7 phage, whose helicase and primase are homologous to the equivalent eubacterial proteins (*19*), the COOH-terminal region of the primase is directly linked to the NH_2-terminal region of the helicase, forming a single polypeptide. Electron micrographs of the phage T7 primase-helicase polyprotein have shown that the helicase region exists as a large hexameric ring, with primase domains arrayed as smaller lobes about one face of the toroid in a 6:6 helicase:primase arrangement (*24*) (Fig. 4, inset). ssDNA appears to be threaded through the interior hole of the ring (*25*), and biochemical studies of the T7 system have suggested a model in which the active site of primase faces outward from the central hole (*26*) (Fig. 4, left). However, a comparison of

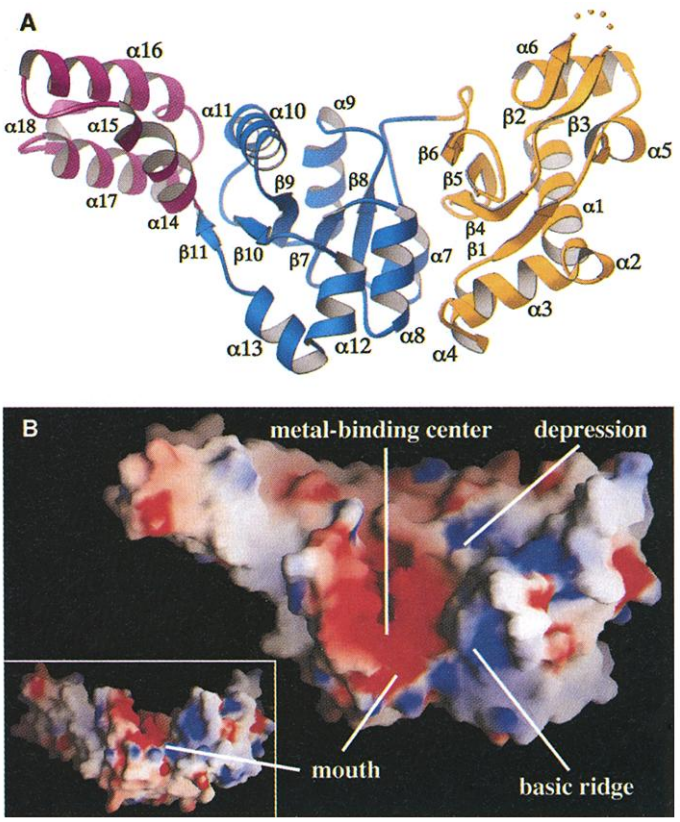

Fig. 2. Structure of DnaG-RNAP. **(A)** Ribbon diagram of the DnaG-RNAP crystal structure, color-coded as in Fig. 1. The toprim region resides in the central (blue) subdomain. Secondary structural elements are labeled as in Fig. 1C and were determined according to standard parameters (*30*). The figure was generated by Ribbons (*27*). **(B)** View of (A) showing the surface potential of DnaG-RNAP. Positive charge potential (+7 k_BT/e) is shown in blue and negative potential (−7 k_BT/e) is shown in red. Acidic, metal-binding residues from the toprim domain and a basic ridge presented by the NH_2-terminal subdomain form the mouth of the putative nucleic acid–binding cleft. The conserved basic depression is also indicated. The figure was generated by GRASP (*31*). (Inset) Side view of (B) rotated by 90°.

the T7 primase-helicase electron micrograph reconstructions with the DnaG-RNAP structure, coupled with the predicted location of the DnaB-ID of DnaG, suggests that an alternative scheme is possible. The COOH-terminus of DnaG-RNAP localizes the DnaB-ID near the region of the DnaG active site that is proposed to bind RNA:DNA hybrid. A DnaB-ID–helicase interaction may therefore

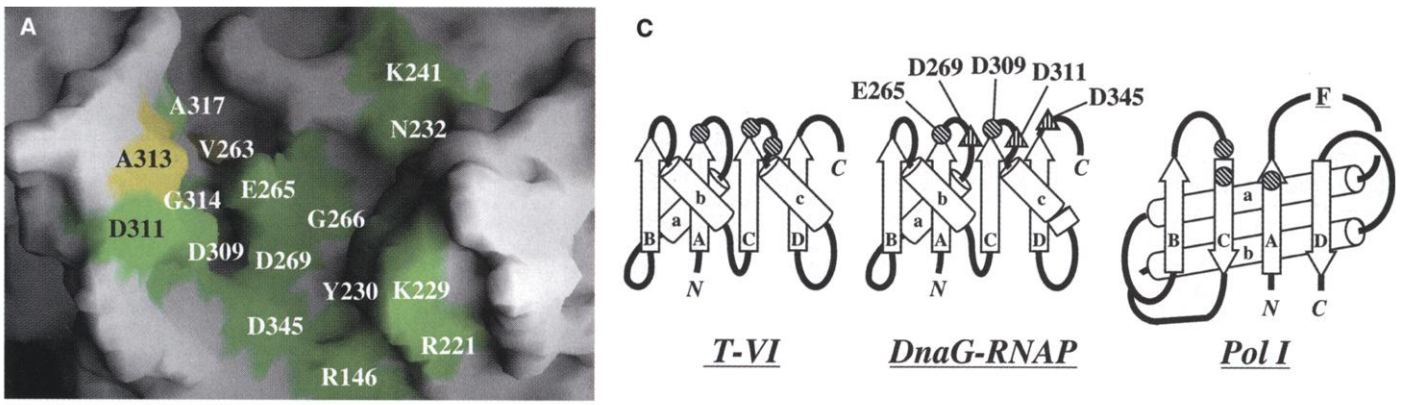

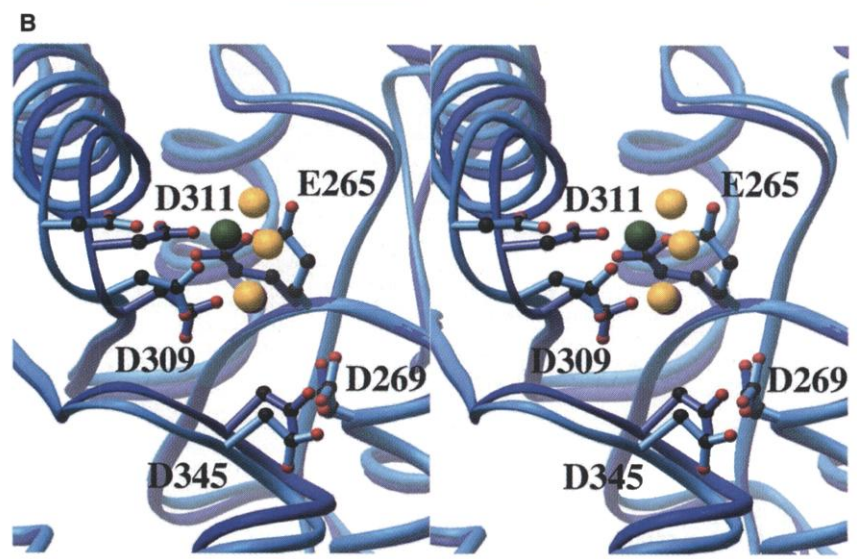

Fig. 3. Catalytic region of DnaG-RNAP. (**A**) Proposed active-site and nucleic acid–binding region of DnaG-RNAP stained to demonstrate locations of all invariant (green) and highly conserved (yellow) surface residues. The figure was generated by GRASP (*31*). (**B**) Stereo diagram of the putative active site of DnaG-RNAP in the unliganded form (light blue) and Y^{2+}-bound form (dark blue). Three Y^{2+} ions are shown as yellow spheres, and a Dy^{3+} ion is shown as a magenta sphere that superposes with the lower Y^{2+} ion. The position of a Mg^{2+} ion bound by the active site of topoisomerase VI (*22*) (green) is overlaid onto DnaG-RNAP by superposition of the homologous toprim domains. One of the Y^{2+} sites lies only 2.5 Å apart from each of the other sites, implying that the observed Y^{2+} sites probably represent an average binding of Y^{2+} ions about the true Mg^{2+}-binding site (or sites) of DnaG. Five invariant-residue side chains are shown: Glu-265, Asp-309 (both Y^{2+}-liganding), Asp-311, Asp-269, and Asp-345. Experimental electron-density maps indicate that these residues are in single rotamer conformations. (**C**) Topology diagrams of the *M. jannaschii* topoisomerase VI (T-VI) (*22*), DnaG-RNAP, and *E. coli* DNA polymerase I Klenow fragment (Pol I) (*32*) metal-binding domains. The orders of secondary-structural elements are indicated alphabetically in lowercase (α helices) and uppercase (β strands) letters. NH_2- and COOH-termini are indicated in italics, and the location of the "fingers" domain in Pol I is indicated as "F". Hatched circles in each diagram indicate invariant metal-liganding residues (Glu-265, Asp-309 in DnaG-RNAP), while triangles indicate the positions of nearby invariant acidic residues (Asp-269, Asp-311, Asp-345). Although the spatial arrangements of metal-binding residues are similar between toprim and palm folds owing to chemical restraints on metal coordination, more detailed comparisons between the active sites await studies of primase-template complexes.

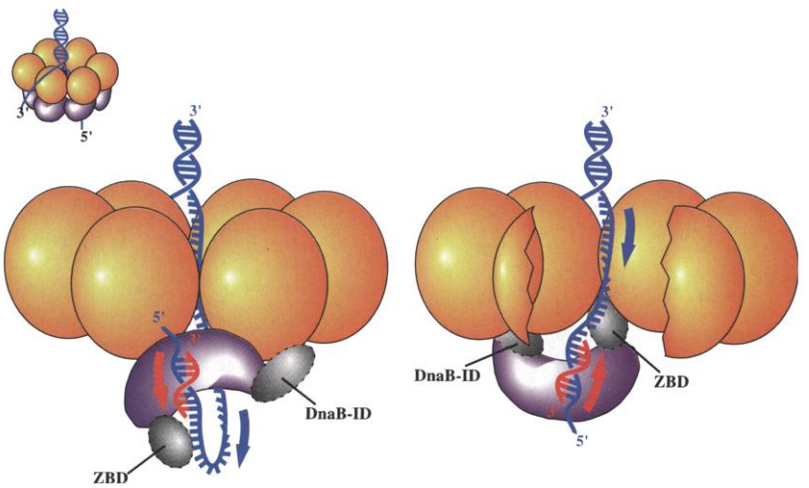

Fig. 4. Model for primase structure and function within the replisome. (**Inset**) Organization of the helicase and primase components of the replisome as observed in the bacteriophage T7 primase-helicase polyprotein (*24*). Primase (purple) directly abuts the helicase (gold). The lagging-strand DNA is thought to be threaded through the central channel (*25*, *33*). (Left and right panels) Models for the orientation of DnaG with respect to DnaB. DNA is shown in blue with synthesized RNA in red. Regions in gray denote the ZBD and DnaB-ID of full-length DnaG whose positions are inferred from the location of the DnaG-RNAP NH_2- and COOH-termini. (**Left**) The primase active site faces away from the central hole of the helicase (*26*). ssDNA extruded from the helicase must loop back to reach the primase active site. The direction by which the RNA:DNA hybrid is translocated and ssDNA is extruded are the same (red and blue arrows, respectively). (**Right**) The DnaG active site faces toward the interior hole of the helicase. Two DnaB protomers have been cut away to show the central hole, where ssDNA from DnaB is guided directly into the DnaG catalytic center for transcription of RNA. The directions of RNA:DNA hybrid translocation and incoming ssDNA are opposed (arrows). Such a model suggests that primer size preferences observed in vitro (*3*) and in vivo (*7*) could arise, in part, from steric effects between the primase, helicase, and newly synthesized primer. The directionality of nucleic acid binding to DnaG is indicated as discussed in the text; although a model where DnaG-RNAP binds primer-template in a different configuration cannot be entirely excluded, existing observations agree with the orientation shown.

place the ssDNA-binding mouth of DnaG distal from DnaB, orienting the active site of primase inward, toward the center of the ring, where it is positioned to accept ssDNA as it is extruded from DnaB (Fig. 4, right). Alternatively, it is possible that mechanistic differences between 6:6 and 6:1 helicase-primase systems lead to different relative orientations of the primase active sites. The true relative locations of these domains awaits high-resolution study of the primase-helicase complexes in *E. coli* and phage T7.

References and Notes

1. D. Brutlag, R. Schekman, A. Kornberg, *Proc. Natl. Acad. Sci. U.S.A.* **68**, 2826 (1971).
2. A. Kornberg and T. A. Baker, *DNA Replication* (Freeman, New York, ed. 2, 1992).
3. E. L. Zechner, C. A. Wu, K. J. Marians, *J. Biol. Chem.* **267**, 4054 (1992).
4. K. Tougu and K. J. Marians, *J. Biol. Chem.* **271**, 21398 (1996).
5. Y. B. Lu, P. V. Ratnakar, B. K. Mohanty, D. Bastia, *Proc. Natl. Acad. Sci. U.S.A.* **93**, 12902 (1996).
6. A. Yuzhakov, Z. Kelman, M. O'Donnell, *Cell* **96**, 153 (1999).
7. T. Kitani, K. Yoda, T. Ogawa, T. Okazaki, *J. Mol. Biol.* **184**, 45 (1985).
8. K. J. Marians, *Annu. Rev. Biochem.* **61**, 673 (1992).
9. K. Tougu, H. Peng, K. J. Marians, *J. Biol. Chem.* **269**, 4675 (1994).
10. W. Sun, J. Tormo, T. A. Steitz, G. N. Godson, *Proc. Natl. Acad. Sci. U.S.A.* **91**, 11462 (1994).
11. J. L. Keck, D. D. Roche, A. S. Lynch, J. M. Berger, data not shown.
12. T5-overexpression plasmids encoding residues 111 to 433 of *E. coli* DnaG (DnaG-RNAP) preceded by a hexahistidine tag were constructed and overexpressed in SG13009/pREP4 cells. Cells were lysed by sonication and the extract was clarified by centrifugation. Soluble DnaG-RNAP was purified by applying the lysate to a nickel-affinity column and eluting the protein with 200 mM imidazole. His-tagged DnaG-RNAP was further purified by size-exclusion chromatography and concentrated to >10 mg ml^{-1}. Selenomethionine-incorporated protein was expressed as described [G. D. Van Duyne, R. F. Standaert, A. P. Karplus, S. L. Schreiber, J. Clardy, *J. Mol. Biol.* **229**, 105 (1993)] and was purified as per the unsubstituted protein, except that 2 mM dithiothreitol was included in all purification buffers. Concentrated His-tagged DnaG-RNAP was dialyzed against 10 mM Hepes (pH 7.5), 100 mM NaCl, and diluted to a final concentration of ~10 mg ml^{-1} before crystallization. Crystals of His-tagged DnaG-RNAP were formed by hanging drop vapor diffusion by mixing 1 μl of protein with 1 μl of well solution [18 to 21% polyethylene glycol (PEG) 4000, 5% PEG200, 30% ethylene glycol, 0.2 M ammonium acetate, 0.05 M sodium acetate (pH 5.0), 0.1% dioxane, 2 to 8 mM $SrCl_2$, YCl_2, or $DyCl_3$] and equilibrating the drop against 1 ml of well solution at room temperature for several days. Two nonisomorphous crystal forms were observed, depending on the divalent metal that was used; with YCl_2 or $DyCl_3$, small platelike crystals (~200 μm by 100 μm by 10 μm) of symmetry $P2_12_12_1$ with unit cell lengths a = 38, b = 56, c = 140 Å were formed; with $SrCl_2$, thicker bar-shaped crystals (~200 μm by 75 μm by 75 μm) of symmetry $P2_12_12_1$ with unit cell lengths a = 39, b = 58, c = 149 Å were formed.
13. Selenomethionine-incorporated $SrCl_2$-based crystals were solved by MAD phasing to 2.5 Å. Data were indexed and scaled with MOSFLM [A. G. W. Leslie, *Newsletter on Protein Crystallography No. 26* (Science and Engineering Research Council, Daresbury Laboratory, Warrington, UK, 1992)] and SCALA [W. Kabash, *J. Appl. Crystallogr.* **21**, 916 (1988)]. Selenium sites were determined with SOLVE [T. C. Terwilliger and J. Berendzen, *Acta Crystallogr. D* **52**, 749 (1996)] and refined with MLPHARE [Z. Otwinowski, *Proc. CCP4 Study Weekend* (Science and Engineering Research Council, Daresbury Laboratory, Warrington, UK, 1991), p. 80]. Solvent-flattening with DM [K. Cowtan, *Joint CCP4 ESF-EACBM Newlett. Protein Crystallogr.* **31**, 34 (1994)] yielded readily interpretable electron-density maps for model building (Fig. 1B) with O [T. A. Jones, J. Y. Zou, S. W. Cowan, M. Kjeldgaard, *Acta Crystallogr. A* **47**, 110 (1991)]. Elves, an automated structure solution package, was used throughout data analysis and map construction (J. Holton and T. Alber, in preparation). The initial model was refined against a high-resolution native data set to 1.6 Å resolution with an R_{work} of 23.1% and an R_{free} of 27.6% by using Refmac/ARP [G. N. Murshudov, A. A. Vagin, E. J. Dodson, *Acta Crystallogr. D* **53**, 240 (1997); V. S. Lamzin and K. S. Wilson, *Acta Crystallogr. D* **49**, 129 (1993)]. The final model includes residues 115 to 428, with the exception of residues 192 to 194 and 287, for which electron density was not observed. No bond angles for this model fall into either disallowed or generously allowed regions of Ramachandrian space.
14. The structure of the YCl_2-based crystal form was solved by molecular replacement with AMORE [J. Navaza, *Acta Crystallogr. D* **50**, 1507 (1994)] and the refined $SrCl_2$ structure as an initial model. The molecular replacement solution was refined to 1.7 Å resolution with an R_{work} of 20.9% and a R_{free} of 26.3% by using Refmac/ARP [G. N. Murshudov, A. A. Vagin, E. J. Dodson, *Acta Crystallogr. D* **53**, 240 (1997); V. S. Lamzin and K. S. Wilson, *Acta Crystallogr. D* **49**, 129 (1993)]. Four Y^{2+} ions were modeled, three of which bound in the putative active site of DnaG-RNAP. The occupancies of these metals were estimated by using $F_o - F_c$ difference maps until the density for these sites was appropriately accounted for. The final model included residues from 115 to 427, excluding residues 192 to 194, for which electron density was not observed. The rmsd for all common C_α atoms between the two structures is 0.6 Å. No bond angles for this model fall into either disallowed or generously allowed regions of Ramachandrian space.
15. L. Holm and C. Sander, *J. Mol. Biol.* **233**, 123 (1993).
16. L. Aravind, D. D. Leipe, E. V. Koonin, *Nucleic Acids Res.* **26**, 4205 (1998).
17. J. M. Berger, D. Fass, J. C. Wang, S. C. Harrison, *Proc. Natl. Acad. Sci. U.S.A.* **95**, 7876 (1998).
18. J. Versalovic and J. R. Lupski, *Gene* **136**, 281 (1993).
19. T. V. Ilyina, A. E. Gorbalenya, E. V. Koonin, *J. Mol. Evol.* **34**, 351 (1992).
20. G. Ziegelin, N. A. Linderoth, R. Calendar, E. Lanka, *J. Bacteriol.* **177**, 4333 (1995).
21. W. Sun, J. Schoneich, G. N. Godson, *J. Bacteriol.* **181**, 3761 (1999).
22. M. D. Nichols, K. DeAngelis, J. L. Keck, J. M. Berger, *EMBO J.* **18**, 6177 (1999).
23. T. A. Steitz, *J. Biol. Chem.* **274**, 17395 (1999).
24. H. H. Egelman, X. Yu, R. Wild, M. M. Hingorani, S. S. Patel, *Proc. Natl. Acad. Sci. U.S.A.* **92**, 3869 (1995).
25. X. Yu, M. M. Hingorani, S. S. Patel, E. H. Egelman, *Nature Struct. Biol.* **3**, 740 (1996).
26. T. Kusakabe, K. Baradaran, J. Lee, C. C. Richardson, *EMBO J.* **17**, 1542 (1998).
27. M. Carson, *J. Appl. Crystallogr.* **24**, 958 (1991).
28. J. D. Thompson, T. J. Gibson, F. Plewniak, F. Jeanmougin, D. G. Higgins, *Nucleic Acids Res.* **25**, 4876 (1997).
29. S. A. Benner, M. A. Cohen, G. H. Gonnet, *Protein Eng.* **7**, 1323 (1994).
30. W. Kabsch and C. Sanders, *Biopolymers* **22**, 2577 (1983).
31. A. Nicholls, K. A. Sharp, B. Honig, *Proteins* **11**, 281 (1991).
32. D. L. Ollis, P. Brick, R. Hamlin, N. G. Xuong, T. A. Steitz, *Nature* **313**, 762 (1985).
33. M. J. Jezewska, S. Rajendran, D. Bujalowska, W. Bujalowski, *J. Biol. Chem.* **273**, 10515 (1998).

34. We thank the 5.0.2 beamline staff at the Advanced Light Source (Lawrence Berkeley National Laboratories) for assistance with measurements and J. Holton and O. Littlefield for helpful discussions. We also thank M. Botchan, R. Calendar, N. Cozzarelli, S. Gradia, R. Fennell-Fezzie, and K. DeAngelis for assistance with the manuscript and E. Egelman for providing electron micrograph reconstructions of the T7 primase-helicase. Supported by the G. Harold and Leila Y. Mathers Charitable Foundation (J.M.B.) and The Jane Coffin Childs Memorial Fund for Medical Research (J.L.K.). The crystallographic coordinates of both structures have been deposited in the RCSB Protein Data Bank (accession codes: 1DD9 and 1DDE).

6 December 1999; accepted 9 February 2000

Mitotic Misregulation and Human Aging

Danith H. Ly,[1] David J. Lockhart,[2] Richard A. Lerner,[1]* Peter G. Schultz[1,2]*

Messenger RNA levels were measured in actively dividing fibroblasts isolated from young, middle-age, and old-age humans and humans with progeria, a rare genetic disorder characterized by accelerated aging. Genes whose expression is associated with age-related phenotypes and diseases were identified. The data also suggest that an underlying mechanism of the aging process involves increasing errors in the mitotic machinery of dividing cells in the postreproductive stage of life. We propose that this dysfunction leads to chromosomal pathologies that result in misregulation of genes involved in the aging process.

The question of why we age has intrigued mankind since the beginning of time. Extensive studies of model systems including yeast, *Caenorhabditis elegans*, *Drosophila*, and mice as well as studies of human progerias and cellular senescence have identified a number of processes thought to contribute to the aging phenotype (*1*). These include the effects of oxidative damage associated with cellular metabolism and genome instabilities such as telomere shortening, mitochondrial mutations, and chromosomal pathologies. To gain greater insights into the mechanisms that control life-span and age-related phenotypes, we have studied gene

[1]Department of Chemistry and the Skaggs Institute for Chemical Biology, The Scripps Research Institute, 10550 North Torrey Pines Road, La Jolla, CA 92037, USA. [2]Genomics Institute of the Novartis Research Foundation, 3115 Merryfield Row, San Diego, CA 92121, USA.

*To whom correspondence should be addressed.